22. J. A. Austin and E. Uchupi, *Am. Assoc. Pet. Geol. Bull.* **66**, 1328 (1982).
23. H. K. Chang, R. O. Kowsmann, A. M. F. Figueiredo, A. A. Bender, *Tectonophysics* **213**, 97 (1992).
24. K. Burke and J. F. Dewey, *J. Geol.* **81**, 406 (1973).
25. M. A. Lanphere and D. L. Jones, in *Contributions to the Geologic Time Scale*, G. Cohee, M. F. Glaessner, H. D. Hedberg, Eds. (American Association of Petroleum Geologists, Tulsa, OK, 1978), pp. 259–268; A. Hallam *et al.*, in *The Chronology of the Geological Record*, N. J. Snelling, Ed. (Blackwell, Palo Alto, CA, 1985), pp. 118–140; T. J. Bralower, K. R. Ludwig, J. D. Obradovich, D. L. Jones, *Earth Planet. Sci. Lett.* **98**, 62 (1990).
26. Y. Bodan, *Phanerozoic Time Scale Bull. Liaison I.U.G.S. Subcomm. Geochronol.* **7**, 31 (1988); G. S. Odin, B. Galbrun, M. Renard, *ibid.* **10**, 39 (1992).
27. This research was supported by the Institute of Human Origins and NSF grants EAR-9209719 to P.R.R. and EAR-8916832 to R.S.C. We are grateful to M. S. D'Agrella for field assistance; R. A. Duncan, D. V. Kent, A. J. Melfi, and A. J. R. Nardy for discussion; G. H. Curtis, R. I. Hill, D. Mertz, E. M. Piccirillo, and M. A. Richards for comments on the manuscript; A. Jaouni and F. Drayer for sample preparation; and D. Beckner for Fig. 1 graphics.

29 June 1992; accepted 9 September 1992

A Prediction of Mars Seismicity from Surface Faulting

Matthew P. Golombek, W. Bruce Banerdt, Kenneth L. Tanaka, David M. Tralli

The shallow seismicity of Mars has been estimated by measurement of the total slip on faults visible on the surface of the planet throughout geologic time. Seismicity was calibrated with estimates based on surface structures on the moon and measured lunar seismicity that includes the entire seismogenic lithosphere. Results indicate that Mars is seismically active today, with a sufficient number of detectable marsquakes to allow seismic investigations of its interior.

The level of tectonic and geologic activity on Mars suggests that it should be seismically more active than the moon but less active than the Earth (*1*). Although the Viking seismometer failed to detect a marsquake, the poor sensitivity of the instrument does not preclude Mars from being a seismically active planet (*2*). In addition, calculations (*1*) indicate that stresses induced by cooling of the martian lithosphere should give rise to seismicity that exceeds the rate of shallow lunar seismicity (28 events in 8 years) thought to be of tectonic origin (*3*).

The seismic scalar moment is defined as $M_o = \mu S A_f$, with uniform rigidity μ and average slip S over fault area A_f. Measurement of the total slip on a fault of known or estimated depth and length allows a determination of the cumulative seismic moment. This value provides an estimate of the total seismic energy released by simple double-couple source mechanisms. The release of the total seismic moment can be distributed according to event size by an assumed relation between moment and frequency of occurrence.

Tectonic features on Mars are found primarily around the Tharsis region, a large elevated volcanic plateau with associated tectonic features that cover the entire western hemisphere of the planet. Tharsis tectonism has occurred mainly during two periods (*4*, *5*), the Late Noachian–Early Hesperian and the Late Hesperian–Early Amazonian. They correspond to time periods of 3.8 to 3.1 billion years ago (Ga) or 4.0 to 3.7 Ga, and 3.1 to 0.7 Ga or 3.7 to 2.5 Ga, respectively, depending on which crater–absolute time scale is used to calibrate martian stratigraphy (*6*). Tectonic features that formed during the first period include (i) a dense radial swarm of narrow grabens, (ii) a sweeping system of concentric wrinkle ridges, (iii) large grabens and rifts of Tempe Terra, and (iv) deep rift valleys of Valles Marineris. Structures that formed during the second period include (i) an enormous set of radial grabens that extend up to thousands of kilometers from the center of the plateau; (ii) large, particularly dense grabens around Alba Patera; (iii) rift zones of Valles Marineris; and (iv) the Thaumasia rift, on the south flank of Tharsis. Tectonism and volcanism continued through the Middle and Late Amazonian (perhaps to the present) at lower levels. Faulting during the Middle Amazonian [0.7 to 0.25 Ga or 2.5 to 0.7 Ga (*6*)] was localized around the center of the plateau and around the large Tharsis Montes volcanoes. Late Amazonian [0.25 or 0.7 Ga to the present (*6*)] faulting surrounded the Tharsis Montes volcanoes and was associated with late stage caldera collapse. Faulting also continued in the rift valleys of Valles Marineris throughout Middle and Late Amazonian time.

The most common tectonic feature on Mars is the simple graben (*7*), which is bounded by two ~60° inward-dipping normal faults (*8*). These faults extend about 2.5 km into the martian interior and have experienced an average of 150 m of slip (*9*). Faulting on narrow grabens has been estimated from a data set (*10*) that includes the locations and lengths of all visible grabens (approximately 7000), about half of which formed during each of the two tectonic periods (*4*, *5*).

Larger grabens and rifts that involve more of the lithosphere are also found on Mars, principally in Valles Marineris, Thaumasia, Tempe Terra, and Alba. Faults bounding the Thaumasia rift (from the Late Hesperian to Early Amazonian periods) and the canyons in Valles Marineris (from both periods) likely extend through the entire brittle lithosphere, estimated to be ~40 km thick (*7*). Slip was determined from the observed topographic relief (4 to 8 km for Valles Marineris, 1.5 km for the Thaumasia rift). Geologic mapping of Valles Marineris (*11*) indicates that trough-bounding faults tens of kilometers long cut Amazonian landslides and floor materials in the canyons and have offset trough walls as much as several hundred meters. On the basis of these relations, the latest fault activity in Valles Marineris during Middle and Late Amazonian time is represented as 20 faults, each 50 km long and having undergone 100 m of slip. Grabens at Alba and Tempe Terra are more narrow and probably involve the upper 5 to 10 km of the lithosphere (*7*). Grabens at Alba formed mostly during the Early Amazonian and have experienced 0.2 to 0.5 km of slip (*12*). Tempe Terra rifts appear to be ~0.5 km deep and were formed in the Late Noachian (*4*). Fault lengths were measured directly from surface maps.

Abundant compressional wrinkle ridges around Tharsis formed during the Early Hesperian. A model in which subsurface thrust faults were assumed to dip about 25° and extend 5 km down dip with ~150 m of slip (*13*) was applied to the lengths of about 2000 ridges around Tharsis (*10*). In addition, the length, average width, and depth of Middle and Late Amazonian grabens were measured to derive fault areas and slips for the two youngest time periods. Caldera collapse also was included in the measurements of Late Amazonian activity because a detailed seismological study (*14*) on Earth shows that collapse occurs by an equivalent shear process and produces fairly large earthquakes. The length, extent [10 km deep (*15*)], and slip [from present relief (*16*)] of circular caldera faults on the tops of Olympus, Ascraeus, Pavonis, and Arsia Mons were included in Late Amazonian

M. P. Golombek, W. B. Banerdt, D. M. Tralli, Jet Propulsion Laboratory, Mail Stop 183-501, California Institute of Technology, Pasadena, CA 91109.
K. L. Tanaka, U.S. Geological Survey, Flagstaff, AZ 86001.

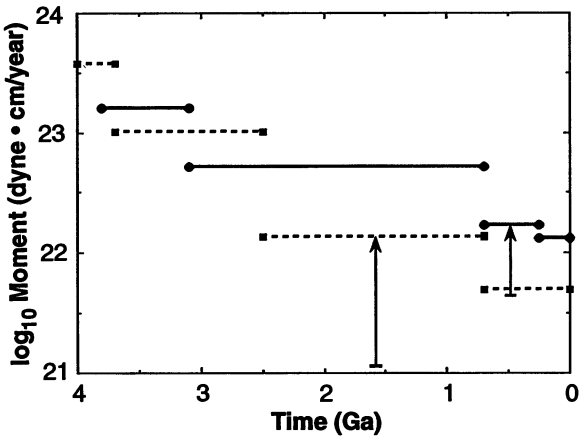

Fig. 1. Plot of the logarithm of cumulative moment release rate through time on Mars, estimated from surface faulting. Solid lines are for the time scale of Hartmann and colleagues in (*6*); dotted lines are for the time scale of Neukum and Wise in (*6*). Arrows show the increase in the estimates for Middle Amazonian moment release rate with the additional contribution inferred from caldera collapse. The total moment release rate during the first two periods is dominated by the contribution from Valles Marineris faults, which have large slip, depth, and length.

Table 1. Predicted recurrence interval of seismic events on Mars.

log (Moment) (dyne·cm)	Terrestrial magnitude	Recurrence interval from surface faulting	Recurrence interval for entire lithosphere
26.5	6.7	35,587 years	356 years
25	5.8	4,484 years	4.5 years
23.5	4.9	565 years	6.8 months
22	4	71 years	0.9 month
20.5	3.1	9 years	3.3 days
19	2.2	1 year	9.8 hours
17.5	1.3	52 days	1.2 hours

activity. Because the volcanoes were also active in the Middle Amazonian (6), a similar level of activity was added to this earlier period. A rigidity of 10^{11} dyne/cm^2 was assumed, on the basis of likely properties of the outer layers of Mars (*4*).

The total moment release per year was greatest during the earliest period of Tharsis deformation and decreased through time to the most recent period (Fig. 1). This decrease appears to follow an exponential decay toward the present, which is expected if seismicity is governed by simple lithospheric cooling. An exponential extrapolation to the present supports the argument that Mars is nearly as seismically active today as it was for the entire Late Amazonian. An estimate of the present moment release rate, inferred from the Late Amazonian (the past 250 million years) is 1.3×10^{22} dyne·cm/year.

To interpret the measured moment release rate in terms of seismicity, relations between moment and frequency of occurrence as well as moment and magnitude were derived from a catalog of intraplate oceanic earthquakes (*17*). Such earthquakes make up a class of seismic events that are thought to be analogous to the type of event expected on Mars [those primarily due to lithospheric cooling and relatively free from plate boundary effects (*1*)].

The distribution of seismic events by moment generally follows a relation of the form

$$N(M_o) = AM_o^{-B} \quad (1)$$

where $N(M_o)$ is the rate of occurrence of events with moment greater than M_o and A and B are constants. The exponent B (0.60, derived empirically from the oceanic event data) governs the relative partitioning of events by moment. The constant A gives the absolute number of events and can be related to the total moment release rate ΣM_o [taking into account the cumulative nature of N (*1*)]:

$$\Sigma M_o = -\int_0^{M_o^*} M_o \frac{dN}{dM_o} dM_o = \frac{AB}{1-B}(M_o^*)^{1-B} \quad (2)$$

where M_o^* is the seismic moment of the largest event.

For $M_o^* = 10^{26.5}$ dyne·cm (based on the largest intraplate oceanic earthquakes) and $\Sigma M_o = 1.3 \times 10^{22}$ dyne·cm (present-day moment release rate from surface faulting), the frequency of occurrence as a function of moment from Eqs. 1 and 2 (Table 1, third column) ranges from tens of marsquakes of moment $\geq 10^{17}$ dyne·cm per year to one marsquake of moment $\geq 10^{26}$ dyne·cm per 10,000 years.

Although seismic moment is the fundamental parameter related to energy release, it is generally easier to judge the size of a seismic event in terms of magnitude. For the purposes of illustration, we converted moment into an equivalent terrestrial body-wave magnitude (m_b) by fitting oceanic intraplate data to a relation between moment and magnitude (*17*) of the form

$$\log M_o = a + bm_b \quad (3)$$

yielding $a = 15.4$ and $b = 1.66$. These magnitudes correspond to the magnitudes that would be determined on Earth for a quake with the given moment (Table 1).

The static moment measured from fault displacements is likely greater than the dynamic moment measured from seismic waveforms because static measurements include pre- and postseismic slip and some aseismic slip. However, other factors suggest that the above estimates of shallow seismicity on Mars are considerably lower than the total seismicity. First, only structures produced by shear faulting visible at the surface today are included; no provision is made for buried or non-shear structures. The estimate also does not include seismic events that do not produce surface displacement (for example, activity associated with hidden faults, deep lithospheric processes, or volcanism) or events due to meteoroid impacts.

On Earth, most earthquakes occur without surface breaks. In an effort to calibrate the estimates based on surface fault slip, we performed a similar calculation for the moon, where results can be compared directly with measured seismicity and moment release for the entire seismogenic lithosphere. This was done by extrapolating to the present the total moment release on the moon from all tectonic features now visible. Grabens on the moon formed from 3.8 to 3.6 Ga (*18*) and mare wrinkle ridges formed from 3.6 to 3.0 Ga (*19*). The cumulative length of grabens on the moon is 17,000 km (*18*). An average slip of 150 m on each of the two bounding 2-km-deep faults for each graben (*20*) results in a cumulative moment release rate of 5.1×10^{21} dyne·cm/year from 3.8 to 3.6 Ga. The cumulative length of mare wrinkle ridges on the moon is ~26,000 km. An average slip of 150 m on 5-km-long thrust faults for each wrinkle ridge (*13*) results in a moment release rate of 3.2×10^{21} dyne·cm/year from 3.6 to 3.0 Ga. If this moment release is extrapolated to the present, on the assumption of an exponential decay, the total moment release rate is $\sim 10^{19}$ dyne·cm/year at present on the moon, a value ~1000 times below that observed for tectonic events on the moon (*21*).

If our estimates for Mars are similarly low, then the present total moment release rate for the entire lithosphere on Mars is about 10^{25} dyne·cm/year, three orders of magnitude higher than estimated from surface faulting alone. This observationally based estimate agrees with theoretical lith-

ospheric cooling calculations for Mars (*1*) and is between the present total moment release rates (*21*) for the moon (10^{22} dyne·cm/year) and the Earth (10^{29} dyne·cm/year), as would be expected from a simple comparison of the geologic and tectonic activity of the planets.

Our results in this paper are quite sensitive to poorly constrained assumptions of the distribution of seismicity (values for B and M_o*) and of the relative contribution of seismicity associated with surface faulting versus that attributable to the entire seismogenic lithosphere. Nevertheless, reasonable assumptions based on applicable data from the Earth and moon imply that Mars is a seismically active planet (Table 1, fourth column). For the total moment release rate for the entire lithosphere and the moment frequency distribution derived earlier, these estimates predict that about two marsquakes of moment $\geq 10^{23.5}$ dyne·cm, about a hundred marsquakes of moment $\geq 10^{20.5}$ dyne·cm, about a thousand marsquakes of moment $\geq 10^{19}$ dyne·cm, and tens of thousands of marsquakes of moment $\geq 10^{17}$ dyne·cm occur per year. The small size of Mars and a number of other factors support the argument that a marsquake equivalent to a body-wave event of magnitude 4 on Earth should be globally detectable by Apollo-class seismometers (*1*). If this statement is true, ~14 teleseismic events and more than a hundred equivalent magnitude 3 or greater earthquakes on Mars would be expected each year. Such events offer a promising prospect for seismological investigations on future missions to Mars.

REFERENCES AND NOTES

1. S. C. Solomon *et al.*, *Technical Report No. 91-02* (Lunar Planetary Institute, Houston, TX, 1991). See R. J. Phillips, *ibid.*, pp. 35–38, for lithosphere cooling calculations and E. A. Okal, *ibid.*, pp. 43–47, for expected seismometer response.
2. D. L. Anderson *et al.*, *J. Geophys. Res.* **82**, 4524 (1977); N. R. Goins and A. R. Lazarewicz, *Geophys. Res. Lett.* **6**, 368 (1979).
3. Y. Nakamura, *Proc. Lunar Planet. Sci. Conf.* 11, 1847 (1980).
4. K. L. Tanaka, M. P. Golombek, W. B. Banerdt, *J. Geophys. Res.* **96**, 15,617 (1991).
5. D. H. Scott and J. M. Dohm, *Proc. Lunar Planet. Sci. Conf.* **20**, 487 (1990).
6. Calibration of martian stratigraphy to two crater-absolute time scales is from K. L. Tanaka [*Proc. Lunar Planet. Sci. Conf.* 17, E139 (1986)]. First interval quoted in text here uses crater time scale of W. K. Hartmann *et al.* [in *Basaltic Volcanism on the Terrestrial Planets* (Pergamon, New York, 1981), pp. 1049–1127]. Second interval quoted in text uses crater time scale of G. Neukum and D. U. Wise [*Science* **194**, 1381 (1976)].
7. W. B. Banerdt, M. P. Golombek, K. L. Tanaka, in *Mars*, H. Keiffer, B. Jakosky, C. Snyder, Eds. (Univ. of Arizona Press, Tucson, in press).
8. P. A. Davis and M. P. Golombek, *J. Geophys. Res.* **95**, 14231 (1990).
9. K. L. Tanaka and P. A. Davis, *ibid.* **93**, 14893 (1988).
10. T. R. Watters and T. A. Maxwell, *Icarus* **56**, 278 (1983).
11. N. E. Witbeck, K. L. Tanaka, D. H. Scott, *U.S. Geol. Surv. Map I-2010* (1991).
12. J. B. Plescia, *J. Geophys. Res.* **96**, 18,883 (1991).
13. M. P. Golombek, J. B. Plescia, B. J. Franklin, *Proc. Lunar Planet. Sci. Conf.* **21**, 679 (1991).
14. J. Filson, T. Simkin, L. J. Leu, *J. Geophys. Res.* **78**, 8591 (1973).
15. P. J. Thomas, S. W. Squyres, M. H. Carr, *ibid.* **95**, 14 345 (1990).
16. P. J. Mouginis-Mark, *Proc. Lunar Planet. Sci. Conf.* **12B**, 1431 (1981); R. J. Pike, *ibid.* **9**, 3239 (1978).
17. E. A. Bergman, *Tectonophysics* **132**, 1 (1986); S. C. Solomon, catalog of 141 oceanic intraplate earthquakes, personal communication.
18. B. K. Lucchitta and J. A. Watkins, *Proc. Lunar Planet. Sci. Conf.* **9**, 3459 (1978).
19. S. C. Solomon and J. W. Head, *Rev. Geophys. Space Phys.* **18**, 104 (1980).
20. M. P. Golombek, *J. Geophys. Res.* **84**, 4657 (1979).
21. J. Oberst, *ibid.* **92**, 1397 (1987); N. R. Goins, A. M. Dainty, M. N. Toksoz, *ibid.* **86**, 378 (1981).

22. Supported by grants from the National Aeronautics and Space Administration Planetary Geology and Geophysics Program to the Jet Propulsion Laboratory, California Institute of Technology, and the U.S. Geological Survey. We thank S. Solomon, R. Phillips, and P. Lundgren for many helpful discussions and for preprints and data in advance of publication. We also thank T. Watters for use of a digitized data set of martian grabens and wrinkle ridges and P. Schenk for use of a computer code to determine the lengths of structures.

21 May 1992; accepted 26 August 1992

Relation Between Long-Term Trends of Oxygen-18 Isotope Composition of Precipitation and Climate

Kazimierz Rozanski, Luis Araguás-Araguás, Roberto Gonfiantini

Stable isotope ratios of oxygen ($^{18}O/^{16}O$) and hydrogen (D/H) in water have long been considered powerful indicators of paleoclimate. However, quantitative interpretation of isotope variations in terms of climate changes is hampered by a limited understanding of physical processes controlling the global isotope behavior. Analysis was conducted of time series of ^{18}O content ($\delta^{18}O$) of monthly precipitation and surface air temperature available through the International Atomic Energy Agency–World Meteorological Organization global network, "Isotopes in Precipitation." This study indicates that long-term changes of isotopic composition of precipitation over mid- and high-latitude regions during the past three decades closely followed long-term changes of surface air temperature with the average $\delta^{18}O$-temperature coefficient around 0.6 per mil per degree Celsius.

Current distribution patterns of deuterium (HDO) and oxygen-18 ($H_2{}^{18}O$) concentrations in meteoric waters (rain and snow) reveal a close relation among some climatically relevant meteorological parameters, such as surface air temperature or amount and isotopic composition of precipitation (*1–6*). These relations have been used in numerous studies to extract paleoclimatic information from records of isotopic composition of ancient precipitation preserved in polar ice cores (*7–12*), carbonate deposits in lakes (*13–15*), ground water (*16–18*), and tree cellulose (*19–21*). Whereas the link between isotope signature of precipitation and climate in polar regions is relatively well understood, this is much less the case in temperate and tropical areas. Doubts have often arisen as to whether spatial relations between isotopic composition of precipitation and climatic variables, derived for current conditions, can be used with confidence to interpret isotope records preserved in various environmental archives because they usually reflect long-term linkage between isotopic composition of precipitation and climate on a given area.

The global survey of oxygen and hydrogen isotope composition of monthly precipitation, initiated in 1961 by the International Atomic Energy Agency (IAEA) in cooperation with the World Meteorological Organization (WMO), provides an opportunity to study the link between isotopic composition of modern precipitation and present climatic conditions on a global scale (Fig. 1). The most important paleoclimatic application is an apparent relation between isotopic composition of precipitation and surface air temperature. Dansgaard (*2*), in his excellent review of the data gathered during the first 3 years of operation of the IAEA/WMO network, noticed that annual mean $\delta^{18}O$ of precipitation was closely related to annual mean surface air temperature for mid- and high northern latitude coastal stations (North Atlantic and Greenland); the slope of the linear fit to the data was 0.69 per mil per degree Celsius. This spatial relation can also be derived from simple models describing the evolution of isotopic composition of atmospheric waters at various stages of the global water cycle (*2, 3, 22–26*). The concept most often applied assumes that rain is formed in isotopic equilibrium with the vapor, at the temperature of the cloud base, and is immediately removed from the cloud (Rayleigh model). Because heavy water molecules ($H_2{}^{18}O$) are preferred in the

International Atomic Energy Agency, 1400-Vienna, Austria.